batteries

MDPI

Article

Ion-Replacement Strategy in Preparing Bi-Based MOF and Its Derived Bi/C Composite for Efficient Sodium Storage

Zhenpeng Zhu [1], Shuya Zhang [1], Kuan Shen [1], Fu Cao [1,*], Qinghong Kong [2] and Junhao Zhang [1,*]

[1] School of Environmental and Chemical Engineering, Jiangsu University of Science and Technology, Zhenjiang 212003, China; zhenpz@163.com (Z.Z.); zhangshuya89@163.com (S.Z.); sk2371785782@163.com (K.S.)
[2] School of the Environment and Safety Engineering, Jiangsu University, Zhenjiang 212013, China; kongqh@ujs.edu.cn
* Correspondence: huanjing2001@163.com (F.C.); jhzhang6@just.edu.cn (J.Z.)

Abstract: To address large volumetric expansion and low conductivity of bismuth-based anodes, an ion-replacement technique is proposed to prepare Bi/C composites, using 1,3,5-benzenetricarboxylicacid (H_3BTC) based metal–organic framework as precursors. The characterizations reveal that the Bi/C composite derived from Cu-H_3BTC is a sheet structure with the size of 150 nm, and Bi nanoparticles are uniformly dispersed in carbon sheets. When assessed as anode material for sodium ion batteries (SIBs), a sheet-like Bi/C anode exhibits superior sodium storage performance. It delivers a reversible capacity of 254.6 mAh g^{-1} at 1.0 A g^{-1} after 100 cycles, and the capacity retention is high at 91%. Even at 2.0 A g^{-1}, the reversible capacity still reaches 242.8 mAh g^{-1}. The efficient sodium storage performance benefits from the uniform dispersion of Bi nanoparticles in the carbon matrix, which not only provides abundant active sites but also alleviates the volume expansion. Meanwhile, porous carbon sheets can increase the electrical conductivity and accelerate the electrochemical reaction kinetics.

Keywords: ion-replacement strategy; sheet-like Bi/C composite; uniform dispersion; sodium-ion batteries; superior cycling stability

Academic Editor: Hirotoshi Yamada

Received: 13 November 2024
Revised: 7 December 2024
Accepted: 19 December 2024
Published: 24 December 2024

Citation: Zhu, Z.; Zhang, S.; Shen, K.; Cao, F.; Kong, Q.; Zhang, J. Ion-Replacement Strategy in Preparing Bi-Based MOF and Its Derived Bi/C Composite for Efficient Sodium Storage. *Batteries* **2025**, *11*, 2. https://doi.org/10.3390/batteries11010002

1. Introduction

Developing intermittent renewable energy sources is an effective strategy to accelerate the "carbon neutral" process. Among them, the key strategy is to develop reliable energy storage devices. Advanced lithium-ion batteries (LIBs) have been successfully used in portable electronic devices and electric vehicles due to the high energy density and long cycle ability [1–3]. However, LIBs are not a permanent solution because lithium and cobalt are scarce and unevenly distributed, which has promoted the development of new rechargeable battery technology. Sodium-ion batteries (SIBs) have the same working mechanism as LIBs, and have the advantages of being inexpensive, abundant in nature, and readily available, thus attracting great attention. Compared with LIBs, Na^+ in SIBs have a larger radius (1.02 Å) and the anode materials of SIBs show a greater volumetric expansion during cycling, which results in slow dynamics and a shortened life span [4]. Therefore, suitable anode materials to effectively withstand the embedding/debedding of Na^+ has become a top priority affecting the development of SIBs [5].

Traditional SIB anode materials include metal oxides, metal sulfides, hard carbon, and other carbon anodes [6–8]. Using graphite as the anode material in LIBs, lithium intercalation into graphite can form a stable binary graphite intercalation compound, but

the interlayer spacing does not match with the larger ionic radius of Na^+, which is not suitable for SIB anode materials. Additionally, many researchers have proposed that a hard carbon anode can show a good cycle life, but they are not applicable for SIBs due to their low initial coulomb efficiency. Metal oxides and metal sulfides generally show a higher theoretical capacity, but they are not the most ideal materials because of their lower conductivity [9]. Fortunately, the ionic conductivity of metal sulfides can be improved by elemental doping [10] and heterostructure design [11]. In recent years, bismuth has become considered as one of the most promising anode materials for SIBs, benefiting from its high theoretical specific capacity (386 mAh g^{-1}), relatively lower reaction voltage (~0.6 V), abundant reserves, and low toxicity [12]. However, when the metal bismuth alloys with sodium, there is a large volume expansion (244%) after reaction, which will make the electrode material fall off from the electrode sheet, resulting in serious capacity attenuation.

To address the poor cyclic stability of bismuth-based anode materials due to the large volume expansion, many strategies have been proposed, such as designing nanostructures, constructing bismuth-based carbon composites, and alloying with other metals (Sn, Sb, Ge, etc.) [13]. It has been proven that the construction of nanostructures is a feasible strategy to slow the volumetric expansion. Additionally, the introduction of a carbon matrix and its combination can also reduce pulverization of bismuth-based anode materials during the cycling process, enhance the electrical conductivity, and inhibit the agglomeration. However, the formation of a nanostructure often requires high temperatures, which can further trigger the self-agglomeration of bismuth in the preparation process [14]. Therefore, it is significant to seek a simple and effective strategy to construct bismuth-based nanostructures with efficient sodium-storage performances.

Metal-organic frameworks (MOFs) mostly exhibit polyhedral structures with high specific surface area, high porosity, and simple and easy-to-obtain synthesis steps, and were often chosen as precursors to prepare porous carbon-based composites [15]. For example, MOF-derived nitrogen-doped porous carbon nanofibers with interconnected channels, which exhibit a high specific capacity of 323 mAh g^{-1} at 0.1 A g^{-1} [16]. In this work, Cu-H_3BTC was selected as the precursor and carbonized, then Bi^{3+} was introduced into the carbon matrix by replacement reaction to obtain the bismuth/carbon (Bi/C) composite. It showed a more stable specific capacity of 254.6 mA h g^{-1} at 1.0 A g^{-1} after 100 cycles and a high reversible capacity of 242.8 mA h g^{-1} at 2.0 A g^{-1}. The superior sodium-storage performances are ascribed to the uniform dispersion of Bi nanoparticles in the carbon matrix and can reduce the stress generated during the discharging/charging process and shorten the ion diffusion distance. Additionally, the sheet-like carbon matrix enhances the electroconductibility and promotes Na^+ diffusion, mitigates the volumetric expansion, and inhibits the structural fragmentation of Bi nanoparticles during cycling [17].

2. Experimental Section

2.1. Materials and Chemicals

Bismuth chloride ($BiCl_3$), copper nitrate hydrate ($Cu(NO_3)_2{\cdot}3H_2O$), methanol (CH_4O), N, N-Dimethylformamide (DMF), 1,3,5-Benzenetricarboxylicacid ($C_9H_6O_6$), and polyvinyl pyrrolidone (PVP) were purchased from China National Medicines Corporation Ltd. (Beijing, China).

2.2. Preparation of Materials

Preparation of the Cu-H_3BTC precursor. Firstly, 0.9 g $Cu(NO_3)_2{\cdot}3H_2O$ and 0.4 g PVP were dissolved sequentially in 50 mL methanol and stirred to get solution A. Subsequently, 0.43 g 1,3,5-benzenetricarboxylic acid was added to 50 mL methanol and stirred until dissolved completely, labeling it solution B. Then, solution B was added dropwise into

solution A and stirred for 0.5 h, left for 24 h before centrifugation, and then dried for 6 h in an oven.

Preparation of the Cu@C composite. The Cu-H_3BTC was placed in a corundum porcelain boat with a lid and put into a tube filled with a H_2/Ar (5% of H_2) atmosphere. Then, the Cu-H_3BTC was subjected to heat treatment at 250 °C for 2 h and heated at 500 °C for 2 h, and the product was Cu@C composite.

Synthesis of the Bi@C composite. The 64 mg Cu@C composite was first dispersed into 20 mL DMF solution by ultrasonication for 20 min. Then, 0.6 mmol $BiCl_3$ was dissolved in 10 mL DMF and added dropwise to the DMF dispersion containing Cu@C composite and stirred for 0.5 h. The obtained solution was then transferred to a 100 mL autoclave and reacted at 100 °C for 12 h, triggering the displacement reaction. After the autoclave cooled, the sample was collected by centrifugation and washing it with DMF and ethanol two times, before being dried in an oven at 60 °C for 12 h. Ultimately, the obtained black product was subjected to heat treatment at 500 °C for 2 h. Additionally, Zn-H_3BTC and Co-H_3BTC precursors were also prepared under the same synthetic route to obtain Bi@C composites as contrast samples.

2.3. Material Characterization

The X-ray diffraction (XRD) patterns were performed on a Smart Lab 9 kW spectrometer with Cu Kα radiation (λ = 1.5406, Å, 5° min^{-1}, 5–85°). A scanning electron microscope (SEM, Philips FEI XL30, The Netherlands) was employed to observe the microscopic shape of samples. The micro-structure and crystal structure were characterized using a transmission electron microscope (TEM, JEOL JEM2100F). The X-ray photoelectron spectroscopy (XPS) experiment was examined using Thermo-Fisher Escalab-250 Xi apparatus. Thermogravimetric (TG) analysis was investigated with a Perkin Elmer Diamond TG/DTA apparatus in O_2 atmosphere at a heating rate of 10 °C/min from room temperature to 800 °C.

2.4. Electrochemical Measurements

LIR2032-type coin batteries were assembled in a glovebox filled with Ar, with less than 0.01 ppm of oxygen and water. When assembling a half battery, the working electrode was prepared by casting a uniform slurry containing 70 wt% active material, 20 wt% Super-P, and 10 wt% carboxymethyl cellulose on Cu foil. The electrodes were dried in a 60 °C vacuum oven for 12 h, then they were punched into a circular plate with the active material of about 1.2 mg cm^{-2}. The metallic sodium foil was used as the counter electrode, the glass membrane was applied as the diaphragm, and 1.0 mol L^{-1} $NaPF_6$ dissolved in diethoxymethane was employed as the electrolyte. The cyclic voltammetry (CV, 0.01–3 V) and electrochemical impedance spectroscopy (EIS, 0.01–100 KHz) measurements were examined on a CHI660D electrochemical workstation. The charge/discharge curves and cycling performances were tested from 0.01 to 3.0 V on LAND CT2001A battery tester.

3. Results and Discussion

The morphologies, structure, and element distribution of Cu-MOF, Cu@C, and Bi@C(Cu) were characterized by SEM, TEM, high resolution TEM (HRTEM), and elemental mapping. Figure 1a shows that the Cu-H_3BTC has an octahedral structure with uniform size and the size of octahedral particles is about 130 nm. After high-temperature calcination, H_3BTC was transformed into a porous carbon skeleton, and the polyhedral structure was still preserved. It is noteworthy that the Cu-H_3BTC polydral structure expands in the process of carbonization [18], as shown in Figure 1b. After the replacement reaction of Bi^{3+}, the SEM image in Figure 1c reveals that the obtained Bi@C (Cu) composite

is a lamellar structure with a size of approximately 150 nm. Moreover, the structure of Bi@C(Cu) changed to a lamellar structure, possibly due to the unequal substitution of Cu and bismuth binding to ligands. The TEM images in Figure 1d further confirm that the product is sheet-like structure, which are consistent with the SEM images in Figure 1c. The HRTEM image in Figure 1e shows that the crystalline interplanar spacing is 0.328 nm, corresponding to the (012) plane of metal Bi. The scanning transmission electron microscopy (STEM) and energy dispersive spectrometer (EDS) in Figures S1 and S2 show that the Bi@C (Cu) composite only includes Bi, C, O, and N elements, and elemental mapping images exhibit that Bi, C, O, and N are uniformly dispersed in the carbon sheets (Figure 1f). As a contrast, Figure S3a shows that Zn-H_3BTC synthesized under the same synthetic conditions also has a polyhedral structure. However, it significantly decreases in size after carbonization, although the product basically retained the polyhedral structure (Figure S3b). It is worth noting that Zn-H_3BTC exhibits a significant difference in size due to a different growth rate from Cu-H_3BTC. After in situ substitution of the carbonized Zn@C composite under the same conditions, it was found that the morphology of the product was irregular, with only a small amount of polyhedral structure (Figure S3c). Figure S3d–f are the SEM images of Co-H_3BTC, Co@C, and Bi@C(Co) composites, which show that the initial Co-H_3BTC has the same polyhedral structure and also exhibits the same nanosize, and the characteristics of the carbonized Co@C surface are consistent with Zn@C. Through further replacement of Bi^{3+}, it is found that Bi@C(Co) composites have the same large size and irregular morphology as Bi@C (Zn) composites.

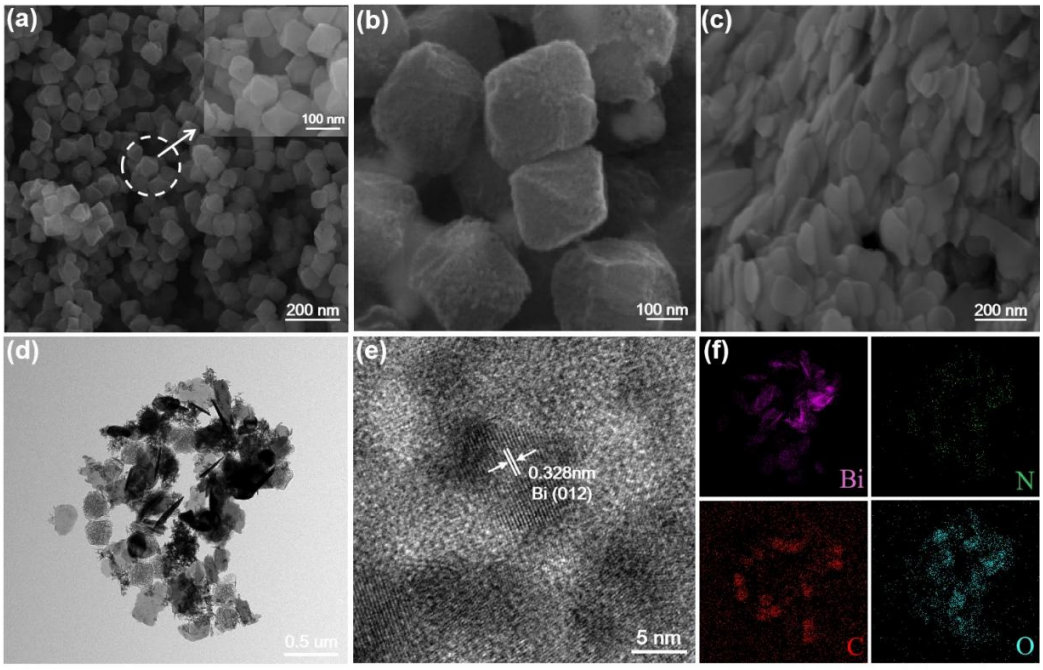

Figure 1. SEM images of Cu-MOF (**a**), Cu@C (**b**), Bi@C(Cu)) (**c**); (**d**,**e**) TEM and HRTEM images of Bi@C(Cu) and (**f**) the corresponding EDS elemental mapping.

To further analyze the phase and composition of Bi@C composites synthesized from different transition metal precursors, XRD patterns were performed on the Bi@C(Cu), Bi@C(Zn), and Bi@C(Co) composites. The XRD patterns in Figure 2a reveal that three composites all show more obvious characteristic peaks at 2θ = 27.5°, 38.1°, and 39.8°, corresponding to the (012), (104), and (110) lattice planes of Bi (JCPDS card No. 44-1246). All characteristic diffraction peaks of copper disappeared after the substitution reaction and convert to those of the metal Bi (JCPDS card No. 44-1246) [19]. Figure 2b shows the TG curve of Bi@C(Cu) in O_2 atmosphere. The results show that a slight weight loss of

5.10 wt% is observed before 237 °C, which is attributed to the release of solvents or water adsorbed during the preparation and storage of the sample [20]. Subsequently, there is a nearly 45 wt% mass loss between 237 °C and 600 °C, which is mainly due to the thermal oxidation of the carbon skeleton in the Bi@C(Cu) composite [21]. When the temperature exceeds 593 °C, the mass of the sample is stable at a certain value, and the content of Bi in the Bi@C(Cu) composite is calculated to be about 36.4 wt%.

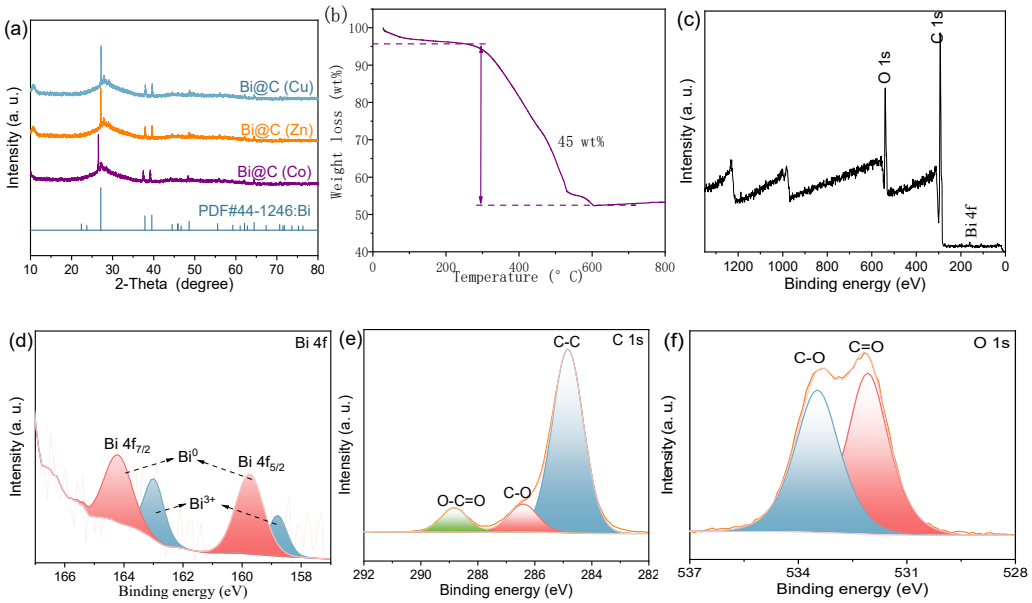

Figure 2. (**a**) XRD patterns of Bi@C(Cu), Bi@C(Zn), and Bi@C(Co); (**b**) TG curves of the Bi@C(Cu) composite; (**c**) XPS Survey spectrum of the Bi@C(Cu) composite; (**d**) Bi 4f; (**e**) C 1s; (**f**) O 1s.

The elemental composition and valence states of the Bi@C(Cu) surface were investigated by XPS. Figure 2c exhibits that the characteristic signal peaks of C 1s, Bi 4f, and O 1s elements can be observed from the XPS survey spectrum. The high-resolution XPS spectrum of Bi 4f in Figure 2d consists of two peaks at 162.1 eV and 158.8 eV, assigning to Bi $4f_{5/2}$ and Bi $4f_{7/2}$ orbitals [22]. From Figure 2e, three fitted peaks of C 1s can be found at 284.8 eV, 286.5 eV, and 288.8 eV, which are assigned to the C-C, C-O and O-C=O bonds [23]. No characteristic peaks of Cu element were found, confirming the successful replacement of Cu by Bi^{3+}. According to Figure 2c,f, there are two obvious O 1s characteristic peaks, deriving from C-O and C=O bonds. The presence of O element is mainly attributed to oxygen-containing groups on the Bi@C(Cu) surface [24].

Figure 3a is the initial four CV profiles of the Bi@C(Cu) anode at 0.1 mV s^{-1} between 0.01 and 3.0 V. In the first cathodic scanning, the multiple broader peaks were found at 0–1.1 V, which is associated with the formation of SEI film and decomposition of electrolytes. The two cathodic scan peaks at 0.48 and 1.13 V are attributed to the multi-step Na-Bi alloying reaction [25]. Except for the first lap, the curves of the second to fourth laps have good overlap and the cathodic peak appearing in the first lap disappears, which indicates that the redox reaction of the Bi@C(Cu) anode has good reversibility and stability, suggesting that an intact and stable SEI film was constructed during the first cycling process [26]. The peak at 0.47 V from the 2nd cathodic scan is derived from the alloying/dealloying process and overpotential change. Two additional cathodic peaks of the second to fourth cathodic scans are observed at 0.75 and 1.23 V, corresponding to the multi-step alloying reaction of Na^+ insertion into Bi to form Na_xBi and the deep sodiation of Na_3Bi. The anodic peaks appearing at 0.63 and 0.83 V represent the phase transition of Na_xBi to Bi [27]. After the formation of a stable SEI film, the anodic peaks of all curves overlap, indicating that the Bi@C(Cu) anode possesses better reversible sodiation/desodiation performance [28]. Figure 3b shows the

charge/discharge curves of Bi@C(Cu) anode for SIBs in the initial five cycles at 1.0 A g^{-1}, and their charge/discharge plateaus are consistent with the cathode and anode peak positions of the CV curves in Figure 3a. The initial capacity of the Bi@C(Cu) anode is 462 mAh g^{-1}, and the Coulombic efficiency is about 89.3%. The curves from the second to fifth laps basically overlap, and their capacitances are in the range of 350.2–382.6 mAh g^{-1}, which indicates that the Bi@C(Cu) anode has a relatively high capacity. Figure 3c provides the rate performances of Bi@C(Cu), Bi@C(Zn), and Bi@C(Co) anodes, and the capacity of the Bi@C(Cu) anode is 511.2, 435.1, 340.2, 280.5, and 242.8 mAh g^{-1} at 0.1, 0.2, 0.5, 1.0, and 2.0 A g^{-1}. When the current density is adjusted to 0.1 A g^{-1} from 2.0 A g^{-1} , the capacity of the Bi@C(Cu) anode still remains 337 mAh g^{-1}, better than those of the Bi@C(Zn) and Bi@C(Co) anodes. The excellent rate performance of the Bi@C(Cu) anode is mainly thanks to the unique sheet-like structure of the Bi@C(Cu) anode that can better reduce the volumetric expansion during the cycling process, favoring the embedding/de-embedding of Na^+ [29]. Figure 3d shows the cycling performances of the Bi@C(Cu), Bi@C(Zn), and Bi@C(Co) anodes at 1.0 A g^{-1}. The results show that the Bi@C(Cu) anode has 254.6 mAh g^{-1} after 100 cycles, with a capacity retention of about 91%, better than those of the Bi@C(Zn) (228 mAh g^{-1}) and Bi@C(Co) (177 mAh g^{-1}) anodes. The better cycling stability of Bi@C(Cu) are attributed to the uniform dispersion of small Bi nanoparticles in the carbon matrix that can provide abundant active sites and relieve volume expansion; meanwhile, porous carbon sheets can increase the electrical conductivity.

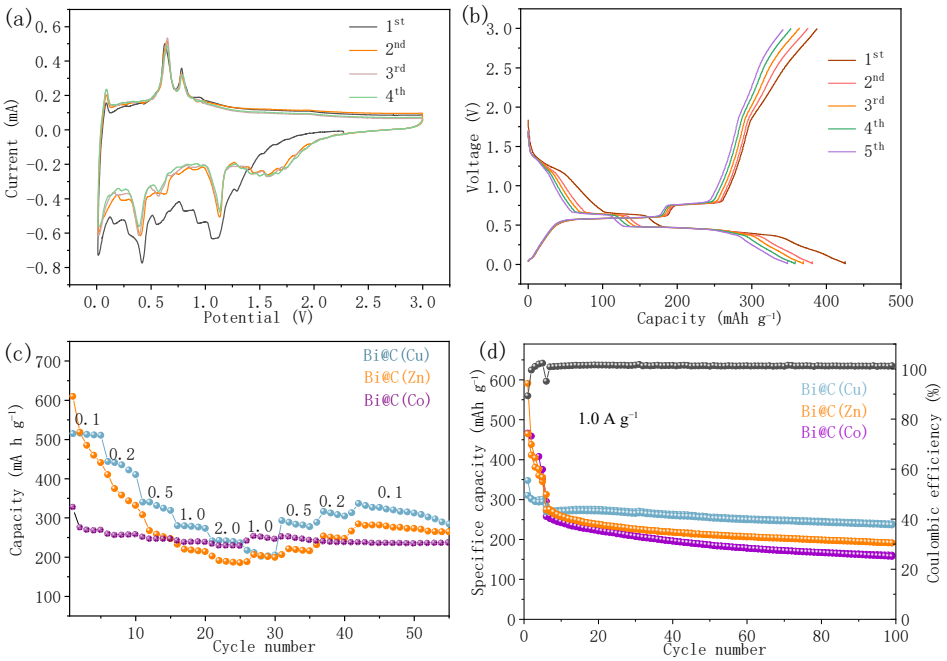

Figure 3. (**a**) CV profiles of the Bi@C(Cu) anode at 0.1 mV s^{-1} between 0.01 and 3.0 V; (**b**) charging/discharging profiles of the Bi@C(Cu) anode at 1.0 A g^{-1}; (**c**) rate performances of the Bi@C(Cu), Bi@C(Zn), and Bi@C(Co) anodes; (**d**) cyclical stability of Bi@C(Cu), Bi@C(Zn), and Bi@C(Co) anodes.

To evaluate the sodium storage capacity of the Bi@C(Cu) anode, kinetic analysis was carried out using cyclic voltammetry from 0.1 to 0.8 mV s^{-1}, as shown in Figure 4a. The peak shapes of all CV curves are similar with obvious peaks and peak position is not offset at gradually increasing sweep rates. The contribution of diffusion and pseudocapacitance for sodium storage can be specifically calculated by equations at the above-mentioned sweep rates [30], as shown in the following relation:

$$i = a\nu^b \quad (1)$$

$$\log(i) = b\log(\nu) + \log(a) \quad (2)$$

where the slope b values are obtained from the log (i) and log (v) plots and a b value near 0.5 or 1.0 represent the sodium storage dynamics which are controlled by diffusion control processes or surface capacitance effects, respectively [31]. Figure 4b provides the values of b for the Bi@C(Cu) anode as 0.96 (peak 1) and 0.83 (peak 2), which are close to 1, confirming that the transition reaction of the Bi@C(Cu) anode is primarily a pseudocapacitive behavior [32]. Figure 4c shows the total capacitance of the Bi@C(Cu) anode to be 0.2 mV s^{-1}, calculated from the integrated area as 65%, which is generated by a pseudocapitance process. The capacitive contribution of the Bi@C(Cu) anode increases significantly with increasing sweep rate (Figure 4d and Figure S4), and the contributions of pseudocapacitance are calculated at different sweep rates, corresponding to 62% (0.1 mV s^{-1}), 65% (0.2 mV s^{-1}), 70% (0.4 mV s^{-1}), and 75% (0.6 mV s^{-1}), respectively. The results indicate that the sodium storage of the Bi@C(Cu) anode is governed by the capacitive effect and dominates over the total charge storage in the electrochemical reaction. The high capacitance contribution favors Na^+ transport, suggesting that the Bi@C(Cu) anode is beneficial for obtaining excellent electrochemical performances, which is attributed to the unique structural feature of the porous sheet-like carbon skeleton [33]. The in situ replacement reaction promotes Bi nanoparticles being firmly anchored to the carbon skeleton, so that more Na^+ could be captured during the electrochemical reaction and electrons could be rapidly transported between Bi and the carbon substrate, thus improving the capacitance contribution of the Bi@C(Cu) anode [34].

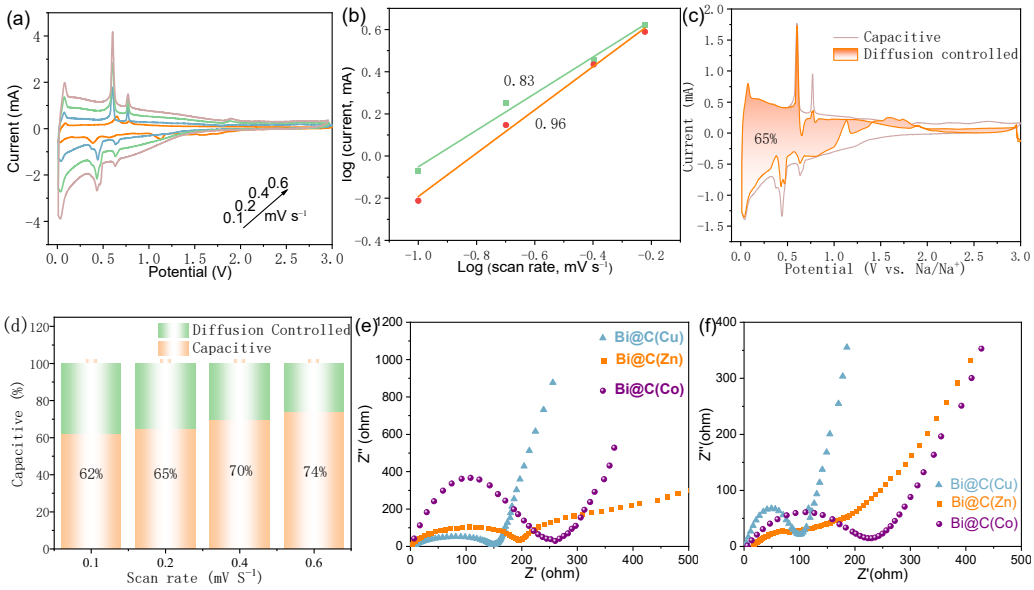

Figure 4. Electrochemical kinetic analysis of the Bi@C(Cu) anode: (**a**) CV profiles from 0.1 to 0.6 mV s^{-1}; (**b**) b-value analysis using the relationship between peak currents and scan rates; (**c**) capacitive contribution of the Bi@C anode at 0.2 mV s^{-1}; (**d**) capacitive contribution at different scan rates; (**e**) EIS of the Bi@C(Cu), Bi@C(Zn), and Bi@C(Co) anodes before cycling; (**f**) EIS of the Bi@C(Cu), Bi@C(Zn), and Bi@C(Co) anodes after 100 cycles.

To further understand the intrinsic reasons for the high sodium storage performances of the Bi@C(Cu) anode, EIS was conducted to study the reaction kinetics. By comparing the ESI before cycling in Figure 4e, the arc radius of the Bi@C(Cu) anode is smaller than those of the Bi@C(Zn) and Bi@C(Co) anodes, illuminating that the Bi@C(Cu) anode has the smallest charge transfer impedance and the fastest charge transfer capability, which is conducive to the fast kinetic properties [35]. Figure 4f shows the EIS of three anodes after 100 cycles at 1 A g^{-1}, and it can be clearly observed that the semicircles of three anodes

in the high-frequency region is obviously narrowed down, meanwhile the charge transfer resistance of the Bi@C(Cu) anode is much lower than those of the Bi@C(Zn) and Bi@C(Co) anodes, indicating that the Bi@C (Cu) anode has the lowest charge transfer resistance. The above results confirm that a Bi nanoparticle embedded in porous carbon nanosheets can greatly enhance the electroconductibility and provide faster charge and ion transport rate for SIBs [36].

To reveal the better cyclical stability of the Bi@C(Cu) anode, the thicknesses and surface structures of the Bi@C(Cu), Bi@C(Zn), and Bi@C(Co) anodes before and after cycling were observed using SEM images. Figure 5a shows that the structures of the Bi@C(Cu) anode piece are intact and compact before cycling, and the thicknesses are 10.7 μm. Figure 5d shows that the thicknesses of the Bi@C(Cu) anode pieces are 14.6 μm after 100 cycles at 1.0 A g^{-1}. According to the calculation, the volume change is ~ 36%. By comparison, the Bi@C(Zn) and Bi@C(Co) anodes have a thickness of 12.5 μm and 13.8 μm before cycling, which are increased to 20.5 μm and 25.1 μm after 100 cycles, as shown in Figure 5b,c,e,f. The Bi@C (Zn) and Bi@C (Co) anodes have expanded by up to 64% and 82%, which are significantly larger values than that of the Bi@C(Cu) anode. Figure S5 shows the SEM images of surface morphologies of the three anodes, which reveal that all three anodes remain intact and are not detached, and the Bi@C(Zn) and Bi@C(Co) anodes show some cracks. The above results further prove that the Bi@C(Cu) anode has a more stable structure than the Bi@C(Zn) and Bi@C(Co) anode, indicating that the sheet-like carbon skeleton of the Bi@C(Cu) anode can effectively release mechanical stress in the process of alloying/dealloying and maintain the structural stability of an anode piece, thus improving the cycle stability of the Bi@C(Cu) anode [37,38].

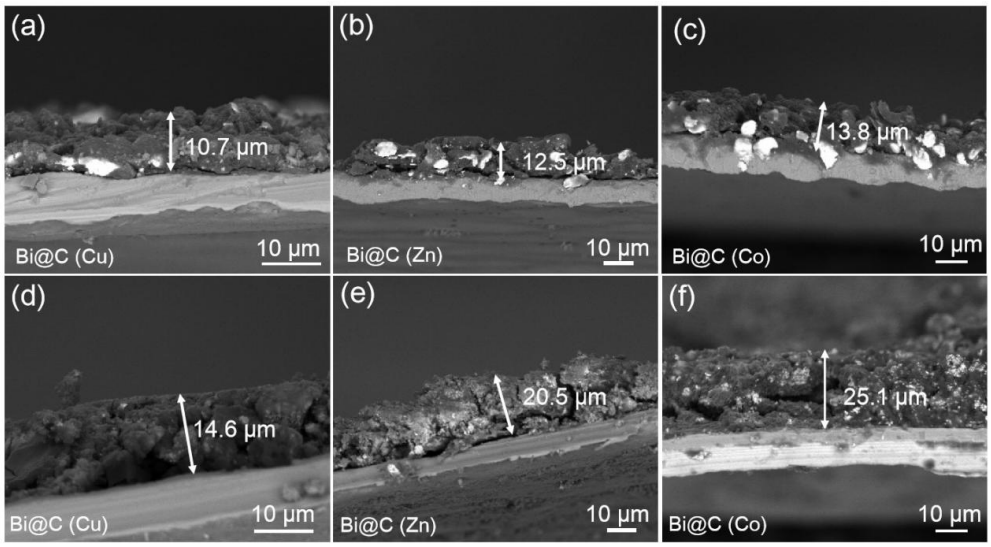

Figure 5. SEM image of the cross section of Bi@C anodes: (**a**) the Bi@C(Cu) anode before cycling; (**b**) the Bi@C(Zn) anode before cycling; (**c**) the Bi@C(Co) anode before cycling; (**d**) the Bi@C(Cu) anode after cycling; (**e**) the Bi@C(Zn) anode after cycling; (**f**) the Bi@C(Co) anode after cycling.

4. Conclusions

In summary, an ion-replacement strategy was proposed to prepare Bi@C composites, using H_3BTC based metal–organic frameworks as precursors. The structural characterization revealed that the Bi@C(Cu) composite was sheet-like in structure with a size of 150 nm, and the Bi nanoparticles were evenly dispersed in carbon sheets. The content of Bi in the Bi@C(Cu) composite was about 36.4 wt%. Evaluated as anode material for SIBs, the Bi@C(Cu) anode exhibited superior sodium storage performance. The initial capacity of the Bi@C(Cu) anode was 462 mAh g^{-1} at 1.0 A g^{-1}, and the Coulombic efficiency was

about 89.3%. Its reversible capacity was 254.6 mAh g^{-1} after 100 cycles at 1.0 A g^{-1}, with a capacity retention of about 91%. Even at 2.0 A g^{-1}, the specific capacities of the Bi@C(Cu) anode reached 242.8 mAh g^{-1}, and it recovered to 337 mAh g^{-1} when the current density was adjusted from 2.0 A g^{-1} to 0.1 A g^{-1}, indicating superior rate ability of the Bi@C(Cu) anode. The efficient sodium storage benefited from the uniform dispersion of Bi nanoparticles in the carbon matrix, which not only provides more active sites, but also alleviates the volume expansion. Meanwhile, porous carbon sheets enhanced the electroconductibility and accelerated the electrochemical reaction kinetics.

Supplementary Materials: The following supporting information can be downloaded at: https://www.mdpi.com/article/10.3390/batteries11010002/s1, Figure S1: STEM image of Bi@C(Cu) composite; Figure S2: EDS of Bi@C(Cu) composite SEM images; Figure S3: (a) Zn-MOF; (b) Zn@C; (c) Bi@C(Zn); (d) Co-MOF; (e) Co@C; (f) Bi@C(Co). Figure S4: contribution of the capacitive-driven process of Bi@C(Cu) anode: (a) 0.1 mV s−1; (b) 0.4 mV s−1; (c) 0.6 mV s−1. Figure S5: SEM images of surface morphologies of the Bi@C anodes: (a) Bi@C(Cu) anode before cycling; (b) Bi@C(Zn) anode before cycling; (c) Bi@C(Co) anode before cycling; (d) Bi@C(Cu) anode after cycling; (e) Bi@C(Zn) anode after cycling; (f) Bi@C(Co) anode after cycling.

Author Contributions: Writing—original draft preparation, Z.Z. and S.Z.; data curation, software, K.S.; formal analysis, project administration, F.C.; investigation, Q.K.; supervision, project administration, and funding acquisition, J.Z. All authors have read and agreed to the published version of the manuscript.

Funding: The research was funded by the National Natural Science Foundation of China (22379056, 22479065), the industry foresight and common key technology research in Carbon Peak and Carbon Neutrality Special Project from Zhenjiang city (CG2023003), and the Industry-University-Research Cooperation Project of Jiangsu Province (BY20230347).

Data Availability Statement: The raw data supporting the conclusions of this article will be made available by the authors on request.

Conflicts of Interest: The authors declare no conflicts of interest.

References

1. Ren, J.; Zhu, H.; Fang, Y.; Li, W.; Lan, S.; Wei, S.; Yin, Z.; Tang, Y.; Ren, Y.; Liu, Q. Typical cathode materials for lithium-ion and sodium-ion batteries: From structural design to performance optimization. *Carbon Neutralization* **2023**, *2*, 339–377. [CrossRef]
2. Zhang, S.; Xue, Y.; Zhang, Y.; Zhu, C.; Guo, X.; Cao, F.; Zheng, X.; Kong, Q.; Zhang, J.; Fan, T. KOH-assisted aqueous synthesis of bimetallic metal-organic frameworks and their derived selenide composites for efficient lithium storage. *Int. J. Min. Met. Mater.* **2023**, *30*, 601–610. [CrossRef]
3. Han, J.; Wang, F. Design and Testing of a small orchard tractor driven by a power battery. *Eng. Agr.* **2023**, *43*, e20220195.
4. Dou, Y.; Zhao, L.; Liu, Y.; Zhang, Z.; Zhang, Y.; Li, R.; Liu, X.; Zhou, Y.; Wang, J.; Wang, J. High-abundance and low-cost anodes for sodium-ion batteries. *Carbon Neutralization* **2024**, *3*, 954–995. [CrossRef]
5. Wang, L.; Zhu, Y.; Du, C.; Ma, X.; Cao, C. Advances and challenges in metal–organic framework derived porous materials for batteries and electrocatalysis. *J. Mater. Chem. A* **2020**, *8*, 24895–24919. [CrossRef]
6. Li, Z.; Wang, S.; Chen, P.; Lei, J.; Hou, Y.; Chen, J.; Zhao, D. Interface Engineering of MOF-Derived Co_3O_4@CNT and CoS_2@CNT Anodes with Long Cycle Life and High-Rate Properties in Lithium/Sodium-Ion Batteries. *ACS Appl. Mater Inter.* **2024**, *16*, 15. [CrossRef]
7. Liu, F.; Zong, J.; Liang, Y.; Zhang, M.; Song, K.; Mi, L.; Feng, J.; Xiong, S.; Xi, B. Ordered vacancies as sodium ion micropumps in Cu-deficient copper indium diselenide to enhance sodium storage. *Adv. Mater.* **2024**, *36*, 202403131. [CrossRef] [PubMed]
8. Zhang, L.; Dong, H.; Lv, C.; Sun, C.; Wei, H.; Miao, X.; Yang, J.; Cao, L.; Geng, H. Electronic structure manipulation of MoSe2 nanosheets with fast reaction kinetics toward long-life sodium-ion half/full batteries. *Inorg. Chem. Front.* **2020**, *9*, 2497–2830. [CrossRef]
9. Qiao, S.; Liu, Y.; Wang, K.; Chong, S. Bismuth Nano-Rods Wrapped with Graphene and N-Doped C as Anode Materials for Potassium- and Sodium-Ion Batteries. *Batteries* **2023**, *9*, 505. [CrossRef]
10. Chen, Y.; Li, S.; Chen, J.; Gao, L.; Guo, P.; Wei, C.; Fu, J.; Xu, Q. Sulfur-bridged bonds enabled structure modulation and space confinement of MnS for superior sodium-ion capacitors. *J. Colloid Interface Sci.* **2024**, *664*, 360. [CrossRef]

11. Song, P.; Yang, J.; Wang, C.; Wang, T.; Gao, H.; Wang, G.; Li, J. Interface Engineering of Fe_7S_8/FeS_2 Heterostructure in situ Encapsulated into Nitrogen-Doped Carbon Nanotubes for High Power Sodium-Ion Batteries. *Nano-Micro Lett.* **2023**, *15*, 118. [CrossRef] [PubMed]
12. Ma, H.; Wang, T.; Li, J.; Yang, J.; Liu, Z.; Wang, N.; Su, D.; Wang, C. Nitrogen doped carbon coated Bi microspheres as high-performance anode for half and full sodium ion batteries. *Chem. Asian J.* **2021**, *16*, 2314–2320. [CrossRef] [PubMed]
13. Sarkar, S.; Roy, S.; Zhao, Y.; Zhang, J. Recent advances in semimetallic pnictogen (As, Sb, Bi) based anodes for sodium-ion batteries: Structural design, charge storage mechanisms, key challenges and perspectives. *Nano Res.* **2021**, *14*, 3690–3723. [CrossRef]
14. Qian, H.; Liu, Y.; Chen, H.; Feng, K.; Jia, K.; Pan, K.; Wang, G.; Huang, T.; Pang, X.; Zhang, Q. Emerging bismuth-based materials: From fundamentals to electrochemical energy storage applications. *Energy Storage Mater.* **2023**, *58*, 232–270. [CrossRef]
15. Liu, S.S.; Zhang, M.M.; Chen, Q.S.; Ouyang, Q. Multifunctional metal-organic frameworks driven three-dimensional folded paper-based microfluidic analysis device for chlorpyrifos detection. *J. Agric. Food Chem.* **2024**, *72*, 14375–14385. [CrossRef] [PubMed]
16. Chu, K.; Hu, M.; Song, B.; Chen, S.; Li, J.; Zheng, F.; Li, Z.; Li, R.; Zhou, J. MOF-derived nitro-gen-doped porous carbon nanofibers with interconnected channels for high-stability Li^+/Na^+ battery anodes. *RSC Adv.* **2023**, *13*, 5634–5642. [CrossRef] [PubMed]
17. Zhou, D.; Wu, T.; Xiao, Z. Self-supported metal-organic framework nanoarrays for alkali metal ion batteries. *J. Alloys Compd.* **2022**, *894*, 162415. [CrossRef]
18. Li, W.; Lee, S.; Manthiram, A. High-nickel NMA: A cobalt-free alternative to NMC and NCA cathodes for lithium-ion batteries. *Adv. Mater.* **2020**, *32*, 2002718. [CrossRef]
19. Zhong, X.; Chen, Y.; Zhang, W.; Zhang, Z.; Li, M. Facile synthesis of a honeycomb-like nano-Bi/N-doped C composite as an anode for sodium-ion batteries with superb cycle stability. *ACS Sustain. Chem. Eng.* **2022**, *10*, 8856–8862. [CrossRef]
20. Yao, T.; Wang, H.; Ji, X.; Zhang, Q.; Meng, L.; Cheng, Y.; Chen, Y.; Han, X. Encapsulation of Titanium Disulfide into MOF-Derived N, S-Doped Carbon Nanotablets Toward Suppressed Shuttle Effect and Enhanced Sodium Storage Performance. *Small* **2024**, *20*, 26. [CrossRef]
21. Guo, C.; Shen, Y.; Mao, P.; Liao, K.; Du, M.; Ran, R.; Zhou, W.; Shao, Z. Grafting of lithiophilic and rlectron-blocking interlayer for garnet-based solid-state Li metal batteries via one-step anhydrous poly-phosphoric acid post-treatment. *Adv. Funct. Mater.* **2023**, *33*, 2213443. [CrossRef]
22. Li, Y.; Song, J.; Ji, Y.; Lu, X.; Tian, Q.; Chen, J.; Sui, Z. Bismuth/bismuth trioxide with a dual-carbon support for high and long life lithium storage. *J. Phys. Chem. Solids* **2022**, *163*, 110562. [CrossRef]
23. Zeng, K.; Wei, W.; Jiang, L.; Zhu, F.; Du, D.L. Use of carbon nanotubes as a solid support to establish quantitative (centrifugation) and qualitative (filtration) immunoassays to detect gentamicin contamination in commercial milk. *J. Agric. Food Chem.* **2016**, *64*, 7874–7881. [CrossRef] [PubMed]
24. Javed, M.; Huang, H.; Ma, Y.R.; Ettoumi, F.E.; Wang, L.; Xu, Y.Q.; El-Seedi, H.R.; Ru, Q.M.; Lou, Z.S. Construction of self-assembled nano cellulose crystals/chitosan nanobubbles composite hydrogel with improved gallic acid release property. *Food Chem.* **2024**, *438*, 137948. [CrossRef] [PubMed]
25. Yang, F.; Yu, F.; Zhang, Z.; Zhang, K.; Lai, Y.; Li, J. Bismuth nanoparticles embedded in carbon spheres as anode materials for sodium/lithium-ion batteries. *Chem. Eur. J.* **2016**, *22*, 2333–2338. [CrossRef] [PubMed]
26. Yang, H.; Chen, L.; He, F.; Zhang, J.; Feng, Y.; Zhao, L.; Wang, B.; He, L.; Zhang, Q.; Yu, Y. Optimizing the void size of yolk–shell Bi@void@C nanospheres for high-power-density sodium-ion batteries. *Nano Lett.* **2020**, *20*, 758–767. [CrossRef] [PubMed]
27. Yuan, H.; Ma, F.; Wei, X.; Lan, J.; Liu, Y.; Yu, Y.; Yang, X.; Park, H.S. Ionic-conducting and robust multilayered solid electrolyte interphases for greatly improved rate and cycling capabilities of sodium ion full cells. *Adv. Energy Mater.* **2020**, *10*, 2001418. [CrossRef]
28. Zhang, W.; Yan, W.; Jiang, H.; Wang, C.; Zhou, Y.; Ke, F.; Cong, H.; Deng, H. Uniform Bi-Sb alloy nanoparticles synthesized from MOFs by laser metallurgy for sodium-ion batteries. *ACS Sustain. Chem. Eng.* **2020**, *8*, 335–342. [CrossRef]
29. Chen, J.; Wang, J.; Zhang, S.; Xue, K.; Zhang, J.; Cao, F.; Kong, Q.; Guo, X. Si nanoparticles confined in N, P-doped double carbon as efficient anode materials for lithium ion batteries. *J. Alloys Compd.* **2023**, *935*, 167850. [CrossRef]
30. Xu, F.; Li, S.; Jing, S.; Peng, X.; Yuan, L.; Lu, S.; Zhang, Y.; Fan, H. Cobalt-vanadium sulfide yolk-shell nanocages from surface etching and ion-exchange of ZIF-67 for ultra-high rate-capability sodium ion battery. *J. Colloid Interface Sci.* **2024**, *660*, 907–915. [CrossRef] [PubMed]
31. Yu, H.; Gao, M.; Zhou, M.; Gu, H.; Zheng, X.; Guo, X.; Liu, Y.; Cao, F.; Kong, Q.; Zhang, J. F127/PDA dual-assisted fabricating high dispersed Ge nanoparticles /N-doped porous carbon composites with efficient lithium storage. *J. Mater. Res. Technol.* **2023**, *26*, 5055–5064. [CrossRef]
32. Zhou, L.; Cao, Z.; Wahyudi, W.; Zhang, J.; Hwang, J.; Cheng, Y.; Wang, L.; Cavallo, L.; Anthopoulos, T.; Sun, Y.; et al. Electrolyte engineering enables high stability and capacity alloying anodes for sodium and potassium ion batteries. *ACS Energy Lett.* **2020**, *5*, 766–776. [CrossRef]

33. Zhang, T.; Wu, M.; Gu, H.; Yu, H.; Zhou, M.; Guo, X.; Liu, Y.; Zheng, X.; Kong, Q.; Zhang, J. Double carbon modified CoS_2/NiS_2 as anode material for efficient lithium storage performance. *J. Energy Storage* **2023**, *73*, 108981. [CrossRef]
34. Wang, X.K.; Pan, Y.; Wang, X.H.; Guo, Y.N.; Ni, C.H.; Wu, J.B.; Hao, C. High performance hybrid supercapacitors assembled with multi-cavity nickel cobalt sulfide hollow microspheres as cathode and porous typha-derived carbon as anode. *Ind. Crop. Prod.* **2022**, *189*, 115863. [CrossRef]
35. Liu, X.; Li, X.; Lu, X.; He, X.; Jiang, N.; Huo, Y.; Xu, C.; Lin, D. Metal-organic framework derived in-situ nitrogen-doped carbon-encapsulated CuS nanoparticles as high-rate and long-life anode for sodium ion batteries. *J. Alloys Compd.* **2021**, *854*, 157132. [CrossRef]
36. Gu, H.; Gao, M.; Zhang, T.; Zhang, J.; Zheng, X.; Guo, X.; Liu, Y.; Cao, F.; Kong, Q.; Xiong, S. F127 assisted fabrication of Ge/rGO/CNTs nanocomposites with three-dimensional network structure for efficient lithium storage. *Chin. Chem. Lett.* **2024**, *35*, 109273. [CrossRef]
37. Xue, K.; Xue, Y.; Wang, J.; Zhang, S.; Guo, X.; Zheng, X.; Cao, F.; Kong, Q.; Zhang, J.; Jin, Z. KOH-assisted aqueous synthesis of ZIF-67 with high-yield and its derived cobalt selenide/carbon composites for high-performance Li-ion batteries. *J. Chem. Eng.* **2023**, *57*, 214–223. [CrossRef]
38. Wu, Q.Q.; Zhong, Y.T.; Chen, R.M.; Ling, G.Y.; Wang, X.H.; Shen, Y.R.; Hao, C. Cu-Ag-C@Ni_3S_4 with core shell structure and rose derived carbon electrode materials: An environmentally friendly supercapacitor with high energy and power density. *Ind. Crop. Prod.* **2024**, *222*, 119676. [CrossRef]